



**HAL**  
open science

## Real-Time Study on Structure Formation and the Intercalation Process of Polymer: Fullerene Bulk Heterojunction Thin Films

Thaer Kassar, Marvin Berlinghof, Nusret Sena Gueldal, Tilo Schmutzler, Federico Zontone, Marco Brandl, Ezzeldin Metwalli, Johannes Will, Ning Li, Tayebbeh Ameri, et al.

### ► To cite this version:

Thaer Kassar, Marvin Berlinghof, Nusret Sena Gueldal, Tilo Schmutzler, Federico Zontone, et al.. Real-Time Study on Structure Formation and the Intercalation Process of Polymer: Fullerene Bulk Heterojunction Thin Films. Solar RRL, 2020, 4 (3), pp.1900508-1-1900508-10. 10.1002/solr.201900508. hal-03725822

**HAL Id: hal-03725822**

**<https://hal.science/hal-03725822v1>**

Submitted on 18 Jul 2022

**HAL** is a multi-disciplinary open access archive for the deposit and dissemination of scientific research documents, whether they are published or not. The documents may come from teaching and research institutions in France or abroad, or from public or private research centers.

L'archive ouverte pluridisciplinaire **HAL**, est destinée au dépôt et à la diffusion de documents scientifiques de niveau recherche, publiés ou non, émanant des établissements d'enseignement et de recherche français ou étrangers, des laboratoires publics ou privés.

# Real-Time Study on Structure Formation and the Intercalation Process of Polymer: Fullerene Bulk Heterojunction Thin Films

Thaer Kassar, Marvin Berlinghof, Nusret Sena Güldal, Tilo Schmutzler, Federico Zontone, Marco Brandl, Ezzeldin Metwalli, Johannes Will, Ning Li, Tayebbeh Ameri, Christoph J. Brabec, and Tobias Unruh\*

Fullerene intercalation between the side chains of conjugated polymers has a detrimental impact on both charge separation and charge transport processes in bulk heterojunction (BHJ) organic photovoltaic cells (OPVs). In situ grazing incidence X-ray scattering experiments allow to characterize the structure formation, drying kinetics, and intercalation in blends of phenyl-c61-butyric acid methyl ester (PC<sub>60</sub>BM) and poly(2,5-bis(3-tetradecylthiophen-2-yl)thieno[3,2-b]thiophene) named (pBTTT-C14) from their 1,2-orthodichlorobenzene (oDCB) solutions with different volume fractions of dodecanoic acid methyl ester (Me12) as a solvent additive. The structure formation process during evaporation of the solvent:additive mixture can be described by five periods, which are correlated to a multistep contraction of the lamellar stacking of the bimolecular crystals. The onset of crystallization is delayed by increasing the additive volume fraction in the coating solution leading to a promoted crystallinity. A conclusive picture of fullerene intercalation and additive-tuned structural evolution during the drying of thin films of the polymer:fullerene BHJ blends will be presented.

## 1. Introduction


Among the variety of renewable energy sources, organic photovoltaic (OPV) cells offer new opportunities for sustainable energy production. Owing to their solution processibility, a cost-efficient fast production through printing on flexible light weight substrates has been realized.<sup>[1,2]</sup> The steadily developing technologies of material design and processing resulted in OPV with over 15.6% power conversion efficiency (PCE).<sup>[3,4]</sup>

Intermixed phases of a conjugated polymer electron donor and an electron-accepting fullerene derivative within the active layer constitute what is referred to as bulk heterojunction (BHJ) OPV cells.<sup>[5]</sup> The tightly Coulomb-bound electron-hole pairs (excitons) generated by light absorption in the polymer are dissociated into free charges at the polymer:fullerene interface. Photocurrent is generated by the collection of the free charge carriers transported through percolation pathways toward the opposite electrodes of the device.

Excitons can diffuse for only 5–10 nm in conjugated polymers to reach a polymer:fullerene interface so they can be split into free charges before recombination of the electron-hole pairs that prevents charge separation.<sup>[6]</sup> Thus, a larger donor:acceptor interfacial area improves exciton splitting, while not fully continuous pathways

throughout the active layer lead to an increased recombination rate of charge carriers as the phases also serve as electron and hole conductors, respectively. Optimizing the exciton diffusion/splitting and extraction of charge carriers, by tuning the nanoscale phase segregation between polymer and fullerene domains, improves the PCE of OPVs.<sup>[7–9]</sup> The extent of this phase separation is determined by the miscibility between acceptor and donor.<sup>[10]</sup> In addition to the domain size and phase distribution, the electronic and optical properties of the active layer are

T. Kassar, M. Berlinghof, T. Schmutzler, Dr. M. Brandl, Dr. E. Metwalli, Dr. J. Will, Prof. T. Unruh  
ICSP (Institute for Crystallography and Structural Physics)  
Friedrich-Alexander University Erlangen-Nürnberg  
Staudtstraße 3, D-91058 Erlangen, Germany  
E-mail: tobias.unruh@fau.de

 The ORCID identification number(s) for the author(s) of this article can be found under <https://doi.org/10.1002/solr.201900508>.

© 2020 The Authors. Published by WILEY-VCH Verlag GmbH & Co. KGaA, Weinheim. This is an open access article under the terms of the Creative Commons Attribution License, which permits use, distribution and reproduction in any medium, provided the original work is properly cited.

DOI: 10.1002/solr.201900508

N. S. Güldal, Dr. N. Li, Prof. C. J. Brabec  
i-MEET (Institute Materials for Electronics and Energy Technology)  
Friedrich-Alexander University Erlangen-Nürnberg  
Martensstraße 7, D-91058 Erlangen, Germany

Dr. T. Ameri  
Department of Physical Chemistry  
University of Munich (LMU)  
Butenandtstraße 11 (E), D-81377 Munich, Germany

Dr. F. Zontone  
European Synchrotron Radiation Facility  
71, avenue des Martyrs, 38043 Grenoble Cedex 9, France

strongly influenced by various structural features such as molecular packing and orientation of the crystalline domains.<sup>[11]</sup>

A higher miscibility between polymer and fullerene can lead to molecularly intermixed phases (either amorphous or bimolecular crystalline).<sup>[12–25]</sup> Bimolecular polymer:fullerene crystals are formed when there is enough space between the side chains of the polymer to accommodate fullerene molecules.<sup>[12–15]</sup> The intercalation of fullerene into the polymer can be controlled by varying the fullerene size or the free volume between the host's side chain.<sup>[16,17,26]</sup>

Donor:acceptor mixing on the molecular level facilitates exciton dissociation, as excitons form within a few angstrom (Å) of a donor:acceptor interface.<sup>[17–21]</sup> However, larger recombination rates were observed in these domains.<sup>[21,22]</sup> Therefore, extended regions (pathways) of either component are necessary for avoiding recombination and efficient charge collection.<sup>[10,27]</sup>

The conjugated semicrystalline polymer poly(2,5-bis(3-alkylthiophen-2-yl)thieno[3,2-b]thiophene), named pBTTT, has been found to be exceptionally suitable to study the nanoscale phase segregation effect on charge generation.<sup>[28–31]</sup> Several fullerene derivatives such as phenyl-C-butyric acid methyl ester (PCBM) can intercalate between the side chains of pBTTT to form a thermodynamically stable BMC (cf. **Figure 1**).<sup>[14]</sup> Its structure is stabilized by van der Waals intermolecular interaction between the polymer and the fullerene molecules.<sup>[32]</sup> The formation of such well-mixed phases prevails over neat domains leading to efficient exciton splitting into free charge carriers that suffer from high recombination rate.<sup>[16,33]</sup> The ratio between the intercalated phase and pure domains of either hole-transporting pBTTT or electron-transporting PCBM can be tuned by varying the composition ratios between pBTTT and PCBM. Anyway, using an excess concentration of one component relative to

the other has resulted in moderate PCEs.<sup>[14,15]</sup> An amorphous intermixed phase has been found to coexist with the BMCs even at relatively low fullerene ratio. Upon thermal annealing, the fullerene molecules diffuse to form large aggregates resulting in phase separation with micrometer length scales and thus low PCE.<sup>[34]</sup> The nanoscale phase segregation can be controlled by using low volatility processing additives.<sup>[35,36]</sup> Due to their high boiling point, additives remain in the film longer than the primary solvent and continue to modulate the blend morphology.<sup>[37]</sup>

Previous studies indicated that using additives such as fatty acid methyl ester offers a possible route for reducing the bimolecular structure within pBTTT:PCBM BHJ films. The asymmetrical additive dodecanoic acid methyl ester (Me12) was chosen, because its polar head favors PCBM while its alkyl tail is attractive to the side chains of pBTTT.<sup>[38–40]</sup>

Grazing incidence X-ray diffraction (GIXD) and grazing incidence small-angle X-ray scattering (GISAXS) have proven to be powerful tools for investigating the structure and morphology of thin film polymer:fullerene BHJ blends.<sup>[37,41,42]</sup> Moreover, time-resolved grazing incidence techniques enable in situ studies of the BHJ morphology evolution during solution processing allowing to gain critical insights into the mechanisms of molecular rearrangements during drying. In a previous work, we shed light on the formation and development of the self-assembled structures in pBTTT:fullerene BHJ systems by monitoring their drying process in real time. The intercalation was found to take place before or during crystallization of the polymer. That resulted in fast drying which completely ends in less than 1 min with the formation of stable BMCs. Their volume remains constant upon subsequent further drying.<sup>[43]</sup>

In this contribution, we present in situ studies of the structure evolution of 1:1 (by weight) pBTTT-C14:PC<sub>60</sub>BM blends processed with Me12 as an additive. By utilizing in situ GISAXS and ex situ GIXD, we characterize the dynamic self-organization and fullerene intercalation that occur during the formation of the complex system.

In our previous work, we presented a custom-made fully automated sample cell designed for full characterization of the processes taking place during thin film drying.<sup>[43]</sup> This cell enables real-time investigations of thin film formation after doctor blading with in situ GIXD/GISAXS measurements complemented by optical techniques such as white light reflectometry and photoluminescence (PL) spectroscopy. It is equipped with an automated system for accurate temperature control and a motorized syringe to inject the sample precursor solution.<sup>[43–46]</sup> The cell has been installed on Beamline ID10 at the European Synchrotron Radiation Facility (ESRF) to monitor the structure formation and drying kinetics of pBTTT-C14:PC<sub>60</sub>BM blends from their 1,2-orthodichlorobenzene (oDCB) solutions with different concentrations of Me12 as a solvent additive. The temperature during the blading process and the measurements was kept constant at 60 °C under an inert atmosphere. The structures of pBTTT, PC<sub>60</sub>BM, Me12, and oDCB are shown in **Figure 2**.

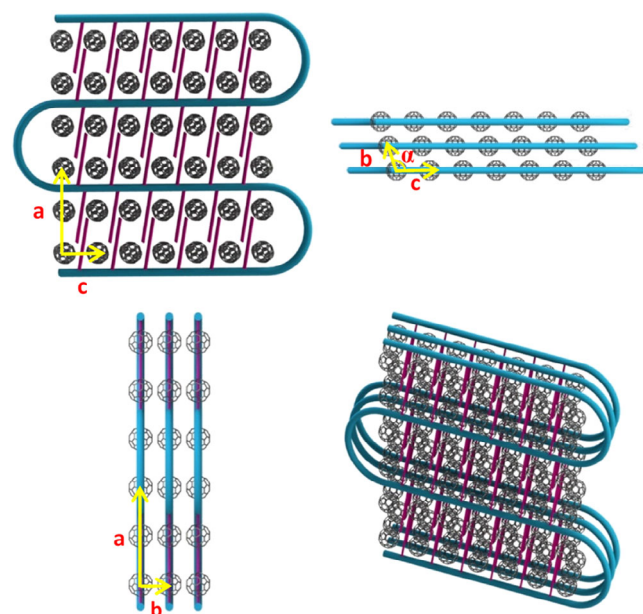


**Figure 1.** Illustrations of pBTTT-C14:PC<sub>60</sub>BM BMCs. The monoclinic unit cell parameters ( $a = 27 \text{ \AA}$ ,  $b = 9.4 \text{ \AA}$ ,  $c = 13 \text{ \AA}$ , and  $\alpha = 108^\circ$ ) based on the observed peaks in our ex situ GIXD measurements and the model proposed in refs. [14,33] are depicted.

## 2. Results and Discussion

OPV BHJ film morphology evolves over a series of periods during its formation upon drying from dilute solutions.<sup>[47]</sup>

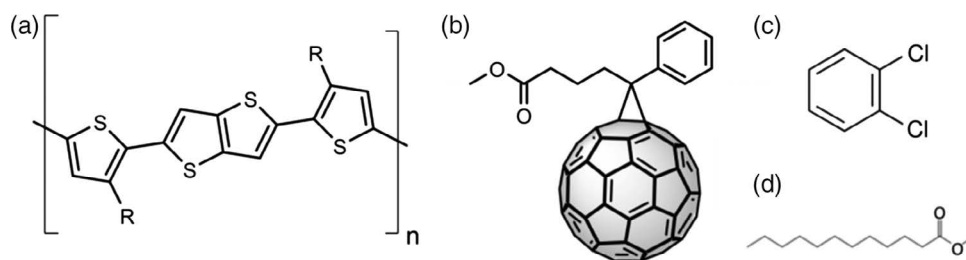


**Figure 2.** The chemical structure of the materials used in this work: a) the pBTTT-C14 variant of pBTTT ( $R = C_{14}H_{28}$ ), b) PC<sub>60</sub>BM, c) the solvent: oDCB, and d) the processing additive: Me12.

The progressive increase in the components' concentration in the solvent is one of the reasons of this multiperiod film formation.<sup>[43,48]</sup> Throughout the course of active layer formation, the concentration of the donor and acceptor increases up to a critical value called solubility limit, at which the corresponding component might start to precipitate.<sup>[42,47]</sup> Unlike fullerenes that show a single solubility limit, conjugated polymers exhibit gelation behavior.<sup>[42]</sup> The fast removal of solvent in the often used "spin coating" processing technique leads to a fast drying process that can also comprise polymer vitrification by fullerene.<sup>[49,50]</sup> Many in situ morphology formation studies focused on the benchmark system P3HT:PCBM. Due to the limited miscibility of P3HT and PCBM, it was assumed that P3HT crystallization leads to squeezing PCBM molecules out of the regions where the polymer crystallizes. Therefore, the phase separation was considered to be driven by P3HT crystallization.<sup>[42,51]</sup> Three main film formation periods, before reaching the final film morphology (glassy state), have been identified<sup>[42,43,47–57]</sup>:

Period 1 (dissolved state): linear thinning rate as the wet film is suffering significant solvent losses

Period 2 (nucleation and growth): starting with the onset of nucleation of the polymer crystalline phase that hinders the diffusion of solvent molecules to the surface leading to a slow solvent evaporation

Period 3 (solvent swollen glassy state): extremely slow evaporation of the residual solvent between the polymer chains leading to a promoted crystallization

The structure formation of intercalating polymer–fullerene blends has been found to be different: The solvent placed between the polymer chains is replaced by the intercalated fullerene molecules. The second drying period is therefore much shorter than that of the intercalation-free blends.<sup>[43]</sup> The interlamellar distances of BMCs (along *a*-axis) exhibit a very limited and quick shrinking in the meantime. However, the in-plane  $\pi$ - $\pi$  stacking (along *b*-axis) and the intramolecular distances (along *c*-axis) do not change at all.<sup>[43]</sup> No further significant changes are likely to happen the third drying period (cf. additive free thin film in **Figure 3**) or upon excessive drying in vacuum. The intercalation was found to take place before or during crystallization of the polymer. That resulted in fast drying which completely ends in less than 1 min with the formation of stable BMCs. Their volume remains constant upon subsequent further drying.<sup>[43]</sup>

In this work, we focused on the additive-driven film structure formation of intercalating polymer:fullerene blends. Morphology evolution of pBTTT-C14:PC<sub>60</sub>BM during the evaporation of

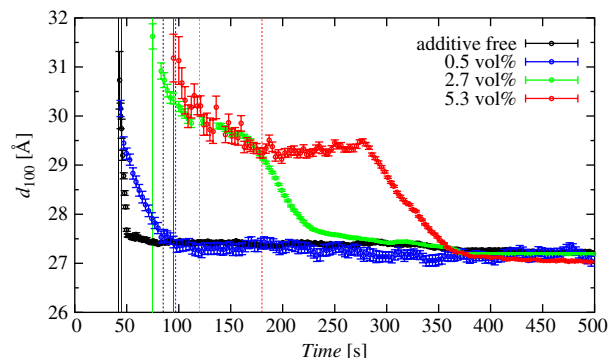


**Figure 3.** Temporal change of the lamellar spacing of pBTTT-C14 crystallites of pBTTT-C14:PC<sub>60</sub>BM blends processed with different amounts of Me12 additive during drying as derived from the time-resolved GISAXS measurements. The vertical solid and dashed lines indicate the onset and end of the second drying period, respectively.

mixed solvents, which comprises host solvent oDCB and processing additive Me12, was investigated by in situ grazing incidence X-ray scattering. The onset of crystallization, i.e., when the lamellar stacking 100 reflection could be observed for the first time, is more delayed with increasing amount of additive as becomes visible from the data, as shown in **Figure 3**. The solubility limit of pBTTT and PCBM in the oDCB:Me12 mixture increases then with increasing volume fraction of the additive, which has a lower vapor pressure compared with oDCB. This onset indicates the end of the first and the beginning of the second drying period. Upon further drying, the 100 reflection shifts to smaller values of the lattice spacing  $d_{100}$  due to the gradual removal of intercalated oDCB and Me12 molecules. In clear contrast to the additive-free film, a multistep contraction of the lamellar stacking has been observed in the films containing higher amounts of Me12 (cf. **Figure 3**). The contraction rate is very high at the beginning of the crystallization and then rapidly slows down. Subsequently, an apparent saturation and afterward a reacceleration are observed which allows to divide the drying process into four distinct temporal periods leading to the final film morphology (period 5), as shown in **Figure 4**. The final  $d_{100}$  is the same for all blends which means that there was no hindrance of fullerene intercalation even for high amounts of Me12. Obviously, the intercalation has occurred prior to or during the polymer crystallization and is present during the very first observation of Bragg reflections of the polymer.

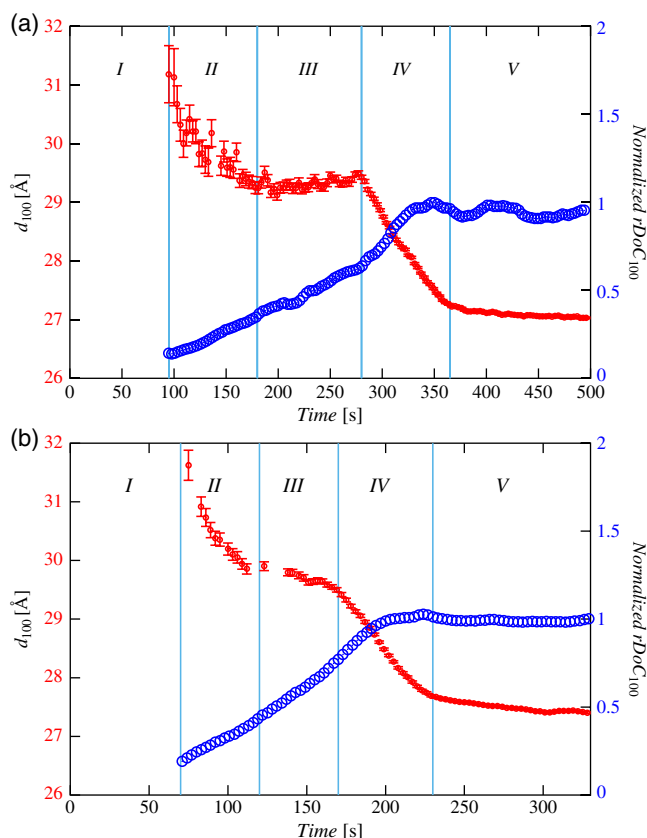


**Figure 4.** Temporal change of the lamellar spacing and relative degree of crystallinity (rDoC) for BMCs of the pBTTT-C14:PC<sub>60</sub>BM blends processed with a) 5.3 vol% and b) 2.7 vol% Me12 additive during drying as derived from the time-resolved GISAXS measurements. Five periods (I–V) of structure development are identified and marked with vertical lines.

To gain more insight into the structure evolution of pBTTT-C14:PC<sub>60</sub>BM blends processed with 5.3 vol% Me12 additive, in-plane and out-of-plane cuts of the time-resolved GISAXS measurements are shown in **Figure 5**. The out-of-plane cuts help to follow the evolution of the Yoneda peak during drying. The in-plane cuts were extracted at the Yoneda peak position at which the GISAXS signal is most pronounced due to the constructive interference phenomenon between the incident and reflected X-ray beam.<sup>[58]</sup> The intensity development of these cuts with time can be followed in the 2D color maps shown in **Figure 5**. The initial film consists of a predominantly liquid phase. The solvent content drops significantly during the first drying period leading to the formation of a strong, broad Yoneda peak. Because of its lower vapor pressure and higher boiling point, Me12 remains in the film longer than oDCB, resulting in a clear change of the material-sensitive Yoneda peak during drying. As shown in **Figure 5**, the in-plane GISAXS scattering intensity increases in the first 50 s and subsequently decreases with increasing drying time. The total scattering invariant (TSI =  $\int I(q)q^2 dq$ )<sup>[59]</sup> has been calculated and is plotted as a function of drying time in **Figure 6a**. The TSI is proportional to the contrast of scattering length densities between the scatterer and the embedding medium and thus to the difference between their indexes of refraction.<sup>[60]</sup> The dispersion term  $\delta$  and the absorption term  $\beta$  of the index of refraction  $n$  for all materials used in this work are shown in Table S1, Supporting Information. The contrast between PC<sub>60</sub>BM and oDCB is the smallest, whereas the biggest contrast is found to be between PC<sub>60</sub>BM and Me12. The TSI increases in the first 50 s of drying due to the essentially sole evaporation of oDCB. The drop of the TSI after the first drying period obviously reflects the evaporation of both Me12 and oDCB and the corresponding increasing volume fraction of pBTTT.

Herein, we introduce a model that is capable of describing the time-resolved GISAXS data in the framework of distorted wave Born approximation (DWBA). In the proposed model,

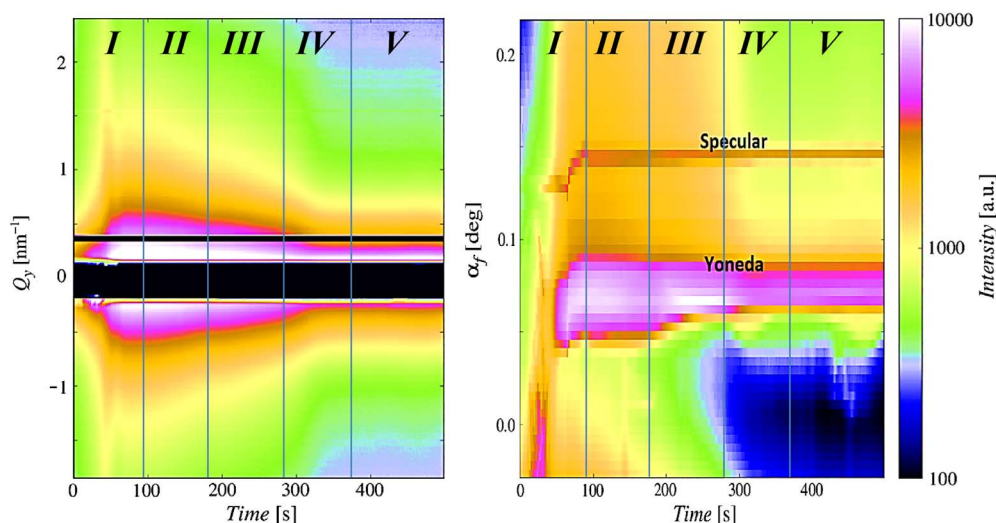


**Figure 5.** In-plane (left) and out-of-plane (right) cuts of the time-resolved GISAXS measurements of pBTTT-C14:PC<sub>60</sub>BM blends processed with 5.3 vol% Me12 additive as a function of the drying time. Five periods (I–V) of structure development are identified and marked with vertical lines.

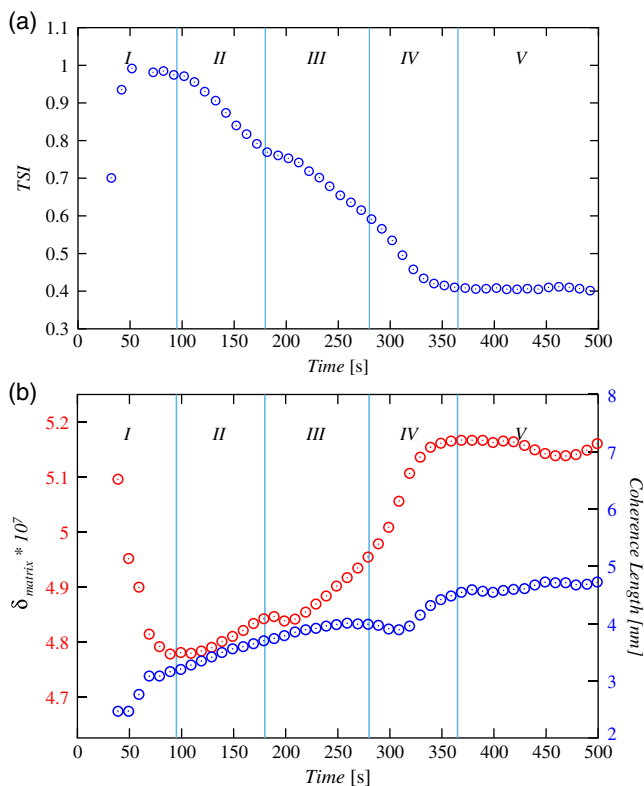


**Figure 6.** a) TSI of the time-resolved GISAXS measurements of pBTTT-C14:PC<sub>60</sub>BM blends processed with 5.3 vol% as a function of the drying time. b) Fit results of the GISAXS intensity using the proposed model:  $\delta_{\text{matrix}}$  (red) and coherence length of the paracrystal (blue). Five periods (I–V) of structure development are identified and marked with vertical lines.

it is assumed that the PC<sub>60</sub>BM molecules are embedded in a matrix consisting of pBTTT, oDCB, and Me12 and exhibit a paracrystalline order in the in-plane direction. The mono-disperse spherical form factor for PC<sub>60</sub>BM molecules ( $R = 0.43 \text{ nm}$ )<sup>[61]</sup> reproduces the broad fullerene halo at ( $q \approx 1.4 \text{ \AA}^{-1}$ )<sup>[62]</sup> in the measured GIXD patterns. To describe the spatial arrangement of fullerene molecules in the film, a radial paracrystal approach according to Hosemann et al. has been chosen as interference function.<sup>[63]</sup> From the lattice parameters of the BMC of pBTTT-C14:PC<sub>60</sub>BM ( $b = 9.4 \text{ \AA}$ ,  $c = 13 \text{ \AA}$ , and  $\alpha = 108$ ),<sup>[14,33]</sup> one can calculate the lateral average distance between PC<sub>60</sub>BM molecules to be 1.235 nm. There is good agreement between the simulation using the proposed model and the experimental data (cf. Figure S1, Supporting Information). More details about the model can be found in the Supporting Information. Figure S2, Supporting Information, shows the simulated GISAXS intensity compared with the experimental data for the completely dried film ( $\delta_{\text{matrix}} = \delta_{\text{pBTTT}}$ ). GISAXS data of pBTTT-C14:PC<sub>60</sub>BM (5.3 vol% Me12) were fitted for each time during drying by adjusting two of the model parameters:  $\delta_{\text{matrix}}$  which alters the scattering contrast and the coherence length  $L$  of the paracrystal (cf. Figure 6b).  $\delta_{\text{matrix}}$  is used to estimate the dynamic volume fraction of all constituents of the film during drying (cf. Table S2, Supporting Information). The results demonstrate that the

temporal evolution of  $\delta_{\text{matrix}}$  is in good agreement with that of the TSI. It decreases in the first drying period as oDCB evaporates and the relative concentrations of Me12 and pBTTT-C14 increase. This results in increased scattering contrast and thus in increase of TSI.  $\delta_{\text{matrix}}$  reaches a minimum at the end of period 1 indicating that Me12 has become the major component of the mixed solvent and just started to evaporate. In period 2, the overall scattering contrast reduces as  $\delta_{\text{matrix}}$  increases due to the evaporation of oDCB and minor amounts of Me12. At the end of this period, the oDCB content vanishes. At this point, the liquid phase consists mainly of pure Me12 due to its vapor pressure being higher than that of oDCB. Now the BMCs with incorporated Me12 are in equilibrium with excess liquid Me12 saturated with solved pBTTT-C14/PC<sub>60</sub>BM. The existence of the corresponding two-phase region was experimentally proven and will be demonstrated later in an independent paragraph. In the third drying period, the liquid Me12 evaporates continuously leading also to recrystallization of pBTTT-C14/PC<sub>60</sub>BM from the solution. This leads to the observed increasing of the relative degree of crystallinity, as shown in Figure 4. According to the phase equilibrium, the  $d_{100}$  value of the BMCs stays constant in this drying period (cf. Figure 4). When all Me12 from the liquid phase has evaporated, only BMCs with cointercalated Me12 embedded in an amorphous pBTTT-C14/PC<sub>60</sub>BM phase are left. Upon further drying and Me12 evaporation in the fourth period, the Me12 concentration in the BMCs decreases which is accompanied by a further reduction of the  $d_{100}$  spacing. When all Me12 is evaporated, pure BMCs are left in the amorphous matrix, and no further changes are observed in the last period. The coherence length increases over the drying time. This increase in lateral size of the BMCs is probably due to particle growth and/or coalescence. It could be also concluded that fullerene intercalation takes place early in the first drying period before the observation of diffraction peaks. This is supported by the in situ PL results (cf. Figure S6, Supporting Information).

The location of Me12 molecules after the complete solvent evaporation and the mechanism underlying its demixing from the ternary pBTTT-C14:Me12:PC<sub>60</sub>BM blend are, however, not well understood. Therefore, transmission small-angle X-ray scattering (SAXS) experiments on the interaction between the additive and the already formed crystals have been conducted. The lamellar spacing of the BMCs as well as of pure pBTTT-C14 crystals manifests a reversible expansion/contraction upon Me12 uptake and release (intercalation and extraction of Me12 molecules; cf. Figure 7 and Figure S3, Supporting Information) Thus, Me12 molecules do intercalate between the side chains of the polymer crystals and along with the already intercalated fullerene molecules in the BMCs. It could be also concluded that Me12 can partly dissolve the BMCs and the amorphous phase resulting in an excess liquid Me12 phase saturated with pBTTT-C14 and PC<sub>60</sub>BM. Extraction of Me12 leads to the recrystallization of the solved pBTTT-C14/PC<sub>60</sub>BM before the contraction of BMCs, as shown in Figure S3, Supporting Information. This supports our drying model presented above respecting the existence of a two-phase equilibrium between liquid Me12 (saturated by pBTTT-C14 and PC<sub>60</sub>BM) and BMCs with intercalated Me12.

We also conducted ex situ GIXD measurements in vacuum at room temperature to study the morphology and molecular packing after the complete removal of additives. The 2D-GIXD detector

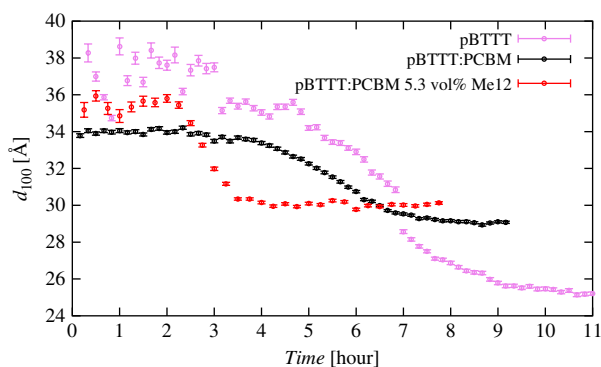


**Figure 7.** The contraction of the lamellar spacing of pBTTT-C14 crystallites upon extraction of Me12 molecules as derived from transmission SAXS. For these measurements, the layers which were previously prepared at the ESRF have been exfoliated from their substrates. They were powdered and filled into capillaries and wetted by a droplet of Me12. The two ends of capillary have been left open to allow a slow removal of Me12 during the measurements performed at 60 °C under vacuum.

images of the completely dried intercalated pBTTT-C14:PC<sub>60</sub>BM films are shown in **Figure 8**. The solvent quality for pBTTT-C14 and PC<sub>60</sub>BM increases with increasing volume fraction of Me12 in the mixed solvent. The use of relatively large amounts of additive seems to enhance the final film crystallinity. In this case, higher-order and mixed-index diffraction peaks are observed and indicate better order of the bimolecular crystalline phase as visible in **Figure 8** and **9**. The Bragg reflections have been indexed according to a standard model proposed elsewhere.<sup>[14,33]</sup> The broad fullerene signature peak at  $q = 1.4 \text{ \AA}^{-1}$  is entangled in a close region with the 700 and the 020 Bragg reflections of the BMC (cf. **Figure S4**, Supporting Information). The promoted crystallization induced by Me12 can be attributed to plasticization of the nearly dry film which extends the time window over which crystallization occurs.<sup>[64–67]</sup> We have found in our previous publication that intercalation results in lower preference for edge-on orientation of crystallites<sup>[43]</sup> presumably due to bulk nucleation.<sup>[68]</sup> This can be attributed to the fast drying as intercalation quenches the liquid film into the glassy state. Nevertheless, BMCs in the blends with large amounts of Me12 have more preference for edge-on orientation than that of the additive-free blend as it becomes obvious from the data shown in **Figure 9** and **S5**. This highly oriented edge-on structure may prevent efficient carrier transport resulting in poor device performance (cf. **Figure S7**, Supporting Information).

Based on the aforementioned discussion, we can propose the following model of the additive-tuned structure formation from solution for intercalating blends:

**Period 1:** Due to its higher vapor pressure, the solvent oDCB evaporates more rapidly than the Me12 additive, resulting in an increased solubility limit of pBTTT-C14 and PC<sub>60</sub>BM in the mixture. This period ends with reaching the critical concentration of pBTTT-C14 in the oDCB:Me12 mixture as evidenced by the earliest observation of polymer crystallization.

The duration of period 1 is found to linearly increase with increasing the amount of additive present in the blend. The additive was found to become the major component in the solvent:additive mixture before the beginning of period 2.

**Period 2:** The 100 diffraction peak originating from the inter-lamellar stacking of the BMC can be observed for the first time at the beginning of this period. The initial BMCs intercalate besides fullerene solvated with Me12 also some oDCB and thus exhibit a large interlamellar spacing. The segregation of oDCB and Me12 molecules from the BMCs with increasing drying time leads to a significant decrease in the interlamellar spacing and an increase in crystallinity.

**Period 3:** oDCB fraction approaches zero leading to a two-phase equilibrium composed of excess liquid Me12 saturated with solved pBTTT-C14/PC<sub>60</sub>BM and BMCs with cointercalated Me12. The drying process continues with the evaporation of liquid phase Me12 and crystallization of the solved pBTTT-C14/PC<sub>60</sub>BM. Me12 intercalated within the BMCs is not yet removed and thus the lamellar stacking is apparently saturated.

**Period 4:** As the residual additive incorporated inside the BMC layers starts to evaporate, the backbone spacing shrinks to its final value leading to a denser packing of the polymer molecules.

**Period 5:** By the complete removal of Me12, the final film morphology is reached.

### 3. Conclusions

In this contribution, in situ structural characterization techniques have been utilized to track the additive-driven film formation of intercalating 1:1 (by weight) pBTTT-C14:PC<sub>60</sub>BM blends from their oDCB solutions with different volume fractions of Me12 as a solvent additive. The structure formation during solvent:additive evaporation subdivides into five temporal periods, which correspond to a multistep contraction of the lamellar stacking of the polymer chains within the BMCs tuned by the amount of additive. Due to its low vapor pressure and high solubility for both pBTTT-C14 and PC<sub>60</sub>BM, Me12 elongates the drying time. Increasing the additive volume fraction in the coating solution delays the onset of crystallization and promotes crystallinity of the BMCs and enhances its edge-on orientation. On the basis of the results, a conclusive picture of the additive-tuned structural evolution during the drying of intercalating polymer:fullerene BHJ blends was presented. The described results demonstrate the importance of in situ structural analysis for developing an in-depth understanding of the formation mechanism in the solution-processed active layers for OSCs.

### 4. Experimental Section

**Materials:** pBTTT-C14 ( $M_w = 40\text{--}80 \text{ kDa}$ ) was purchased from Lumtec (Taiwan), whereas PC<sub>60</sub>BM (99.5%) was purchased from Solenne (the Netherlands) and used without further purification. pBTTT-C14:PC<sub>60</sub>BM solutions (1:1 by mass) were prepared in 1,2-orthodichlorobenzene (oDCB) (99%) purchased from Sigma-Aldrich (Germany). The total concentrations of the pBTTT-C14:PC<sub>60</sub>BM mixture were  $30 \text{ mg mL}^{-1}$ . Dodecanoic acid methyl ester (Me12) (99.5%) was purchased from Sigma-Aldrich. All solutions were left stirring for more than 4 h at 100 °C to fully dissolve all compounds. The films were prepared by doctor blading at 60 °C. As GIXD/GISAXS and PL techniques require an ultraflat and a well-characterized substrate, films were deposited onto silicon substrates purchased from Si-Mat (Germany) with natural SiO<sub>2</sub>. The wafers were cut into rectangular pieces (20 mm × 80 mm), cleaned mechanically

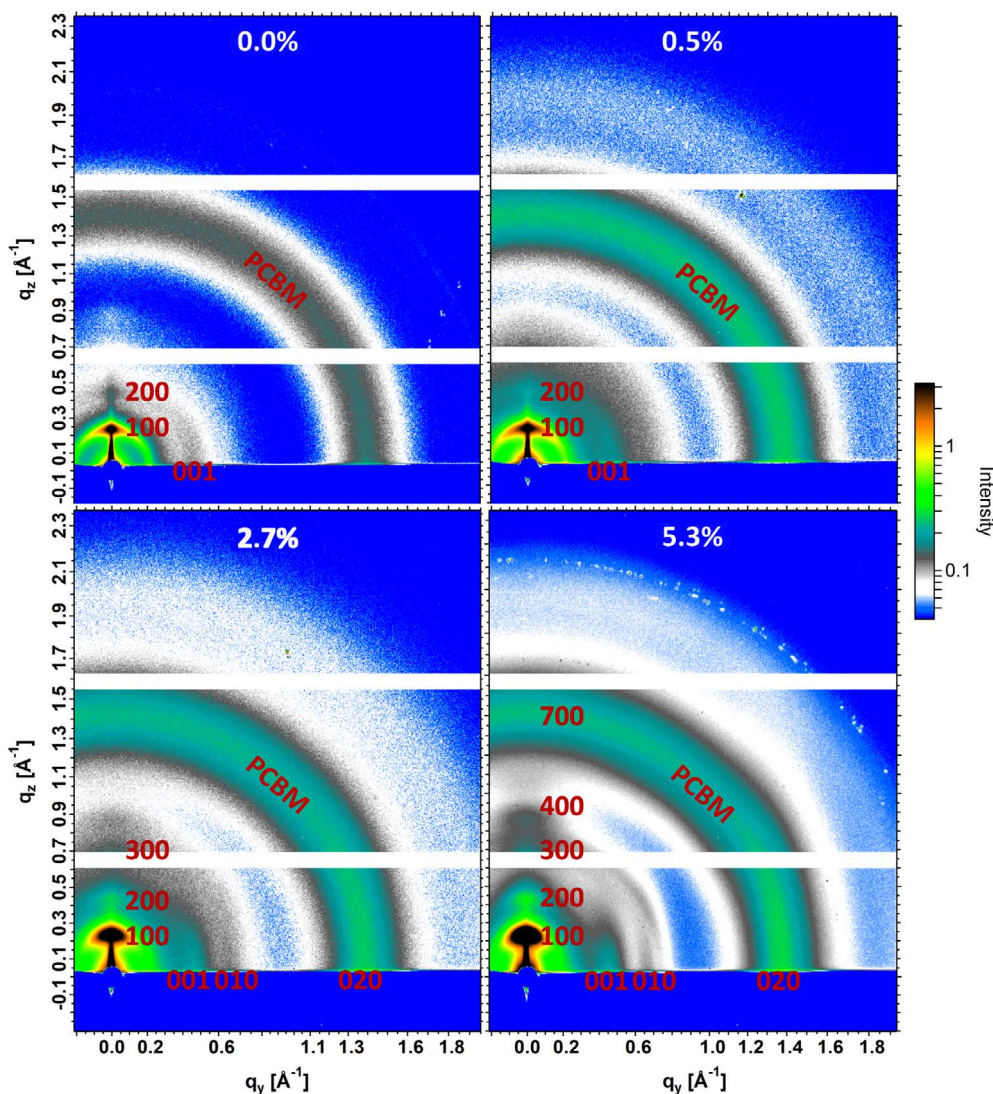


**Figure 8.** Ex situ GIXD detector images of the completely dried films of pBTTT-C14:PC<sub>60</sub>BM processed with different amounts of Me12 additive measured with the VAXSTER instrument. Regions in white correspond to the position of the two intermodule gaps of the Pilatus detector. A beam stop was used to avoid oversaturation of the detector.

with soapy deionized water, rinsed with deionized water, and ultrasonicated with acetone and then with isopropanol. The substrates were dried with nitrogen and kept in a desiccator to avoid any contamination on the surface.

**In Situ GISAXS:** The in situ GISAXS measurements were carried out at the ID10 beamline of the ESRF (France) using a high spatial resolution MAXIPIX area detector (516 pixel × 516 pixel) with a pixel size of 55 μm × 55 μm. The detector-to-sample distance was calibrated to be 663.2 mm with a silver behenate standard. An evacuated flight tube has been installed between the cell and the detector to reduce the air scattering. The measurements were carried out with an X-ray energy of 22 keV. GISAXS data were collected with an incidence angle of 0.14° to obtain a clear separation between the critical angles of the involved materials and the specular peak. To obtain information about the crystalline structures with a weak background from the substrate, an incidence angle of 0.07° was selected. Grazing incidence geometry of the incident X-ray with respect to the sample surface had been used to enhance the scattered intensity, to maximize the scattering volume, and to access the 3D structure of the studied thin films (lateral and normal direction). About 50 μL of

sample precursor solution were dispensed by the motorized syringe under the edge of the doctor blade adjusted 300 μm above the substrate surface. The in situ measurements commenced immediately after the solutions were injected using an automatized injection system on precleaned silicon substrates at 60 °C under a dry helium atmosphere. The blade was immediately translated after injection at a velocity of 15 mm s<sup>-1</sup>. The beamline slits were adjusted to produce a vertically 10 μm-wide beam which illuminated the full length of the 20 mm-long substrate. The footprint at the sample position was roughly 20 mm × 0.204 mm. Any radiation damage was avoided by dividing the measurement into 500 frames and horizontally moving the whole cell 20 μm per frame. Therefore, the total measured sample area was 1 × 2 cm<sup>2</sup>. The X-ray exposure time was adjusted to be 0.995 s per frame. As 20 μm horizontal movement of the cell took 0.005 s, the frame time was 1 s. At the beginning of the coating process, the applicator blocks the incident X-ray beam. Respecting that the distance between the blade and the beam blocking frame of the applicator is 15 mm, the first time frame of the recorded X-ray data with full scattering intensity corresponds to a time of 15 mm / (15 mm s<sup>-1</sup>) = 1 s after film formation. Data were reduced using DPDAK software.<sup>[69]</sup> GISAXS data analysis was



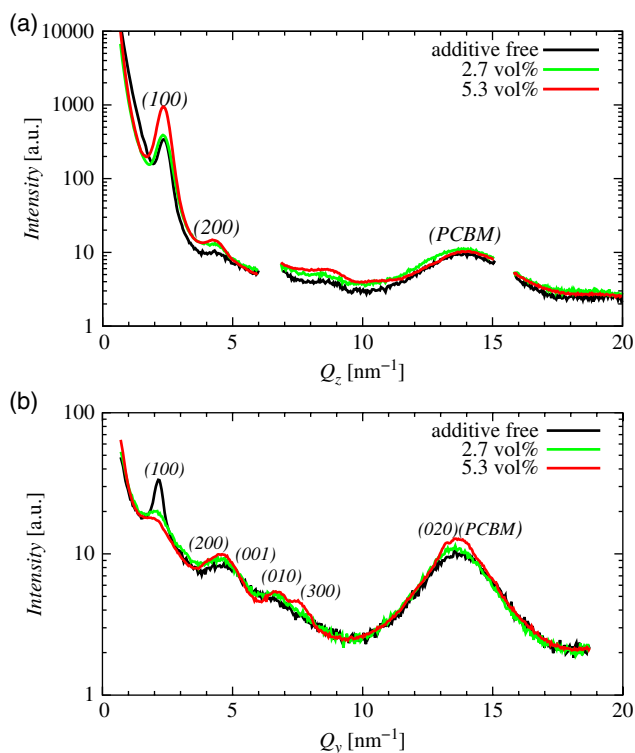


**Figure 9.** a) Out-of-plane and b) in-plane cuts of the ex situ GIXD detector images of the completely dried films of pBTTT-C14:PC<sub>60</sub>BM processed with different amounts of Me12 additive. The missing parts of the curves in (a) correspond to the two intermodule gaps of the Pilatus detector where no photons can be counted.

based on the DWBA<sup>[70]</sup> using the BornAgain software package<sup>[71]</sup> and taking the form and structure factor of particles embedded in the film as well as reflection and refraction effects into account.

**Ex Situ GIXD:** In addition to the in situ measurements, 2D-GIXD measurements of the dried thin films prepared at the ESRF have also been recorded for reference. For this purpose, the apparently dried samples at the end of an in situ drying experiment were dried in vacuum to reduce the solvent content in the samples as far as possible before performing the 2D-GIXD measurement. The ex situ measurements were carried out inside the fully evacuated beam path of the highly customized Versatile Advanced X-ray Scattering instrument ERLangen (VAXSTER) at the Institute for Crystallography and Structural Physics (Friedrich-Alexander-Universität Erlangen-Nürnberg, Germany). The beam was shaped by two of the four available automated double-slit systems (aperture sizes  $0.7 \times 0.7$  and  $0.4 \times 0.4 \text{ mm}^2$ , respectively) with a distance of about 1.2 m between the two. The second slit system consisted of four “scatter-less” silicon single crystal blades. All ex situ measurements were carried out at 22 °C inside the fully evacuated beam path using a 2D Pilatus3 300 K detector (Dectris AG, Switzerland). The collimation line was tilted and shifted with respect to the horizontal plane allowing grazing incidence angles which maximize the scattering volume and enhance the scattered intensity. The measurements were carried out with X-ray energy of 9.25 keV (Ga K $\alpha$ ) and an incidence angle  $\alpha_i$  of about 0.17°. The sample-detector distance (SDD) was calibrated to be 172.5 mm using a silver behenate standard, providing a footprint of about  $0.5 \times 20 \text{ mm}^2$  at the sample position.

**SAXS:** SAXSpace from Anton Paar GmbH (Austria) was utilized in this work for SAXS measurements at the Institute for Crystallography and Structural Physics (Friedrich-Alexander-Universität Erlangen-Nürnberg, Germany). X-rays were provided by a Cu K $\alpha$  microfocus tube (50 W)

and detected by a 2D diode-array (CMOS) detector (Pilatus 100k, Dectris AG, Switzerland) with  $172 \times 172 \mu\text{m}^2$  pixel size. The X-ray beam intensity was enhanced and monochromatized by a focusing multilayer mirror. The sample holder was equipped with a silica glass capillary with an inner diameter of  $\approx 1 \text{ mm}$  and  $10 \mu\text{m}$  wall thickness. The thin films prepared at the ESRF had been mechanically exfoliated by a scraper and transported to the capillaries. A droplet of Me12 had been injected into each capillary. The two ends of capillary had been left open to allow removal of Me12 during the measurements performed at 60 °C under vacuum. The SDD was calibrated to be 306 mm using a silver behenate standard.

## Supporting Information

Supporting Information is available from the Wiley Online Library or from the author.

## Acknowledgements

The authors gratefully acknowledge the funding of the Deutsche Forschungsgemeinschaft (DFG) through INST 90/825-1 FUGG, INST 90/751-1 FUGG, INST 90/827-1 FUGG, the “Cluster of Excellence Engineering of Advanced Materials (EAM),” the research training group GRK 1896 “In situ Microscopy with Electrons, X-rays and Scanning Probes,” the research unit FOR 1878 “Functional Molecular Structures on Complex Oxide Surfaces,” and the funding of the German Federal Ministry of Education and Research (BMBF, project numbers 05K16WEB and 05K16WE1). The authors thank the “European Synchrotron Radiation Facility” ESRF for granting the beam time and appreciate the support of Karim Lhoste and Oleg Konovalov at the beamline ID10. The authors thank Christian Bär, Herbert Lang, and Jürgen Grasser from the workshop of the Institute for Crystallography and Structural Physics (ICSP) at FAU for the construction of the in situ sample cell. The authors declare no competing financial interest.

## Conflict of Interest

The authors declare no conflict of interest.

## Keywords

additives, fullerenes, intercalation, organic solar cells, thin films

Received: November 7, 2019

Revised: December 19, 2019

Published online: January 24, 2020

- [1] C. J. Brabec, N. S. Sariciftci, J. C. Hummelen, *Adv. Funct. Mater.* **2001**, 11, 15.
- [2] C. W. Tang, *Appl. Phys. Lett.* **1986**, 48, 183.
- [3] J. Yuan, Y. Zhang, L. Zhou, G. Zhang, H.-L. Yip, T.-K. Lau, X. Lu, C. Zhu, H. Peng, P. A. Johnson, M. Leclerc, Y. Cao, J. Ulanski, Y. Li, Y. Zou, *Joule* **2019**.
- [4] The National Renewable Energy Laboratory of the U.S. Department of Energy, Best Research-Cell Efficiency Chart, <http://www.nrel.gov/pv/cell-efficiency.html> (accessed: June 2019).
- [5] G. Yu, A. J. Heeger, *J. Appl. Phys.* **1995**, 78, 4510.
- [6] C. J. Brabec, S. Gowrisanker, J. J. M. Halls, D. Laird, S. Jia, S. P. Williams, *Adv. Mater.* **2010**, 22, 3839.
- [7] B. A. Collins, J. R. Tumbleston, H. Ade, *J. Phys. Chem. Lett.* **2011**, 2, 3135.

- [8] T. M. Clarke, J. R. Durrant, *Chem. Rev.* **2010**, *110*, 6736.
- [9] W. Chen, M. P. Nikiforov, S. B. Darling, *Energy Environ. Sci.* **2012**, *5*, 8045.
- [10] B. A. Collins, E. Gann, L. Guignard, X. He, C. R. McNeill, H. Ade, *J. Phys. Chem. Lett.* **2010**, *1*, 3160.
- [11] C. J. Brabec, M. Heeney, I. McCulloch, J. Nelson, *Chem. Soc. Rev.* **2011**, *40*, 1185.
- [12] N. C. Cates, R. Gysel, Z. Beiley, C. E. Miller, M. F. Toney, M. Heeney, I. McCulloch, M. D. McGehee, *Nano Lett.* **2009**, *9*, 4153.
- [13] N. C. Miller, E. Cho, R. Gysel, C. Risko, V. Coropceanu, C. E. Miller, S. Sweetnam, A. Sellinger, M. Heeney, I. McCulloch, J.-L. Brédas, M. F. Toney, M. D. McGehee, *Adv. Energy Mater.* **2012**, *2*, 1208.
- [14] A. C. Mayer, M. F. Toney, S. R. Scully, J. Rivnay, C. J. Brabec, M. Scharber, M. Koppe, M. Heeney, I. McCulloch, M. D. McGehee, *Adv. Funct. Mater.* **2009**, *19*, 1173.
- [15] N. C. Miller, R. Gysel, C. E. Miller, E. Verploegen, Z. Beiley, M. Heeney, I. McCulloch, Z. Bao, M. F. Toney, M. D. McGehee, *J. Polym. Sci. Polym. Phys.* **2011**, *49*, 499.
- [16] N. C. Miller, S. Sweetnam, E. T. Hoke, R. Gysel, C. E. Miller, J. A. Bartelt, X. Xie, M. F. Toney, M. D. McGehee, *Nano Lett.* **2012**, *12*, 1566.
- [17] W. L. Rance, A. J. Ferguson, T. McCarthy-Ward, M. Heeney, D. S. Ginley, D. C. Olson, G. Rumbles, N. Kopidakis, *ACS Nano* **2011**, *5*, 5635.
- [18] N. C. Cates, R. Gysel, J. E. P. Dahl, A. Sellinger, M. D. McGehee, *Chem. Mater.* **2010**, *22*, 3543.
- [19] W. Yin, M. Dadmun, *ACS Nano* **2011**, *5*, 4756.
- [20] N. Banerji, *J. Mater. Chem. C* **2013**, *1*, 3052.
- [21] T. J. Savenije, W. J. Grzegorzczuk, M. Heeney, S. Tierney, I. McCulloch, L. D. A. Siebbeles, *J. Phys. Chem. C* **2010**, *114*, 15116.
- [22] A. Baumann, T. J. Savenije, D. H. K. Murthy, M. Heeney, V. Dyakonov, C. Deibel, *Adv. Funct. Mater.* **2011**, *21*, 1687.
- [23] D. R. Kozub, K. Vakhshouri, L. M. Orme, C. Wang, A. Hexemer, E. D. Gomez, *Macromolecules* **2011**, *44*, 5722.
- [24] D. Chen, F. Liu, C. Wang, A. Nakahara, T. P. Russell, *Nano Lett.* **2011**, *11*, 2071.
- [25] N. D. Treat, C. G. Shuttle, M. F. Toney, C. J. Hawker, M. L. Chabinyc, *J. Mater. Chem.* **2011**, *21*, 15224.
- [26] E. K. Burnett, B. P. Cherniawski, S. J. Rosa, D.-M. Smilgies, S. Parkin, A. L. Briseno, *Chem. Mater.* **2018**, *30*, 2550.
- [27] C. K. Lee, C. W. Pao, *J. Phys. Chem. C* **2012**, *116*, 12455.
- [28] D. M. DeLongchamp, R. J. Kline, A. Herzing, *Energy Environ. Sci.* **2012**, *5*, 5980.
- [29] B. H. Hamadani, D. J. Gundlach, *Appl. Phys. Lett.* **2007**, *91*, 243512.
- [30] M. L. Chabinyc, M. F. Toney, R. J. Kline, I. McCulloch, M. Heeney, *J. Am. Chem. Soc.* **2007**, *129*, 3226.
- [31] D. Alberga, A. Perrier, I. Ciofini, G. F. Mangiatordi, G. Lattanzi, C. Adamo, *Phys. Chem. Chem. Phys.* **2015**, *17*, 18742.
- [32] S. Sweetnam, K. Vandewal, E. Cho, C. Risko, V. Coropceanu, A. Salleo, J. L. Brédas, M. D. McGehee, *Chem. Mater.* **2016**, *28*, 1446.
- [33] N. C. Miller, E. Cho, M. J. N. Junk, R. Gysel, C. Risko, D. Kim, S. Sweetnam, C. E. Miller, L. J. Richter, R. J. Kline, M. Heeney, I. McCulloch, A. Amassian, D. AcevedoFeliz, C. Knox, M. R. Hansen, D. Dudenko, B. F. Chmelka, M. F. Toney, J.-L. Brédas, M. D. McGehee, *Adv. Mater.* **2012**, *24*, 6071.
- [34] W. Zhang, H. Shen, B. W. Guralnick, B. J. Kirby, N. A. Nguyen, R. Remy, C. F. Majkrzak, M. E. Mackay, *Sol. Energy Mater. Sol. Cells* **2016**, *155*, 387.
- [35] J. Peet, J. Y. Kim, N. E. Coates, W. L. Ma, D. Moses, A. J. Heeger, G. C. Bazan, *Nat. Mater.* **2007**, *6*, 497.
- [36] F. Machui, P. Maisch, I. Burgués-Ceballos, S. Langner, J. Krantz, T. Ameri, C. J. Brabec, *ChemPhysChem* **2015**, *16*, 1275.
- [37] N. Shin, L. J. Richter, A. A. Herzing, R. J. Kline, D. M. DeLongchamp, *Adv. Energy Mater.* **2013**, *3*, 938.
- [38] E. Buchaca-Domingo, A. J. Ferguson, F. C. Jamieson, T. McCarthy-Ward, S. Shoaee, J. R. Tumbleston, O. G. Reid, L. Yu, M.-B. Madec, M. Pfannmöller, F. Hermerschmidt, R. R. Schröder, S. E. Watkins, N. Kopidakis, G. Portale, A. Amassian, M. Heeney, H. Ade, G. Rumbles, J. R. Durrant, N. Stingelin, *Mater. Horiz.* **2014**, *1*, 270.
- [39] F. Dou, E. Buchaca-Domingo, M. Sakowicz, E. Rezasoltani, T. McCarthy-Ward, M. Heeney, X. Zhang, N. Stingelin, C. Silva, *J. Mater. Chem. C* **2015**, *3*, 3722.
- [40] H. S. Marsh, A. Jayaraman, *J. Polym. Sci. B Polym. Phys.* **2015**, *53*, 1046.
- [41] G. Li, Y. Yao, H. Yang, V. Shrotriya, G. Yang, Y. Yang, *Adv. Funct. Mater.* **2007**, *17*, 1636.
- [42] B. Schmidt-Hansberg, M. Sanyal, M. F. G. Klein, M. Pfaff, N. Schnabel, S. Jaiser, A. Vorobiev, E. Müller, A. Colmann, P. Scharfer, D. Gerthsen, U. Lemmer, E. Barrena, W. Schabel, *ACS Nano* **2011**, *5*, 8579.
- [43] T. Kassar, N. S. Güldal, M. Berlinghof, T. Ameri, A. Kratzer, B. C. Schroeder, G. L. Destri, A. Hirsch, M. Heeney, I. McCulloch, C. J. Brabec, T. Unruh, *Adv. Energy Mater.* **2016**, *6*, 1.
- [44] N. S. Güldal, T. Kassar, M. Berlinghof, T. Ameri, A. Osvet, R. Pacios, G. L. Destri, T. Unruh, C. J. Brabec, *J. Mater. Chem. C* **2016**, *16*.
- [45] N. S. Güldal, M. Berlinghof, T. Kassar, X. Du, X. Jiao, M. Meyer, T. Ameri, A. Osvet, N. Li, G. L. Destri, R. H. Fink, H. Ade, T. Unruh, C. J. Brabec, *J. Mater. Chem. A* **2016**, *13*.
- [46] M. Berlinghof, C. Bär, D. Haas, F. Bertram, S. Langner, A. Osvet, A. Chumakov, J. Will, T. Schindler, T. Zech, C. J. Brabec, T. Unruh, *J. Synchrotron Radiat.* **2018**, *25*, 1.
- [47] T. Wang, A. D. F. Dunbar, P. A. Staniec, A. J. Pearson, P. E. Hopkinson, J. E. MacDonald, S. Lilliu, C. Pizzey, N. J. Terrill, A. M. Donald, A. J. Ryan, R. A. L. Jones, D. G. Lidzey, *Soft Matter* **2010**, *6*, 4128.
- [48] E. S. Radchenko, D. V. Anokhin, K. L. Gerasimov, A. I. Rodygin, A. A. Rychkov, E. D. Shabratova, S. Grigorian, D. A. Ivanov, *Soft Matter* **2018**, *14*, 2560.
- [49] K. W. Chou, B. Yan, R. Li, E. Q. Li, K. Zhao, D. H. Anjum, S. Alvarez, R. Gassaway, A. Biocca, S. T. Thoroddsen, A. Hexemer, A. Amassian, *Adv. Mater.* **2013**, *25*, 1805.
- [50] P. Westacott, J. R. Tumbleston, S. Shoaee, S. Fearn, J. H. Bannock, J. B. Gilchrist, S. Heutz, J. DeMello, M. Heeney, H. Ade, J. Durrant, D. S. McPhail, N. Stingelin, *Energy Environ. Sci.* **2013**, *6*, 2756.
- [51] P. Kohn, Z. Rong, K. H. Scherer, A. Sepe, M. Sommer, P. Müller-Buschbaum, R. H. Friend, U. Steiner, S. Hüttner, *Macromolecules* **2013**, *46*, 4002.
- [52] S. Pröllner, F. Liu, C. Zhu, C. Wang, T. P. Russell, A. Hexemer, P. Müller-Buschbaum, E. M. Herzig, *Adv. Energy Mater.* **2016**, *6*, 1.
- [53] L. H. Rossander, N. K. Zawacka, H. F. Dam, F. C. Krebs, J. W. Andreasen, *AIP Adv.* **2014**, *4*.
- [54] M. Sanyal, B. Schmidt-Hansberg, M. F. G. Klein, C. Munuera, A. Vorobiev, A. Colmann, P. Scharfer, U. Lemmer, W. Schabel, H. Dosch, E. Barrena, *Macromolecules* **2011**, *44*, 3795.
- [55] M. Sanyal, B. Schmidt-Hansberg, M. F. G. Klein, A. Colmann, C. Munuera, A. Vorobiev, U. Lemmer, W. Schabel, H. Dosch, E. Barrena, *Adv. Energy Mater.* **2011**, *1*, 363.
- [56] X. Gu, H. Yan, T. Kurosawa, B. C. Schroeder, K. L. Gu, Y. Zhou, J. W. F. To, S. D. Oosterhout, V. Savikhin, F. Molina-lopez, C. J. Tassone, S. C. B. Mannsfeld, C. Wang, M. F. Toney, Z. Bao, *Adv. Energy Mater.* **2016**, *6*, 1.
- [57] Z. Bi, H. B. Naveed, Y. Mao, H. Yan, W. Ma, *Macromolecules* **2018**, *51*, 6682.
- [58] A. N. Nigam, *Phys. Rev. A* **1965**, *138*, 1189.

- [59] L. J. Richter, D. M. DeLongchamp, F. A. Bokel, S. Engmann, K. W. Chou, A. Amassian, E. Schaible, A. Hexemer, *Adv. Energy Mater.* **2015**, 5, 1.
- [60] A. Guinier, G. Fournet, *Small Angle Scattering of X-Rays*, John Wiley & Sons, New York, NY **1955**.
- [61] A. Ruzsinszky, J. P. Perdew, J. Tao, G. I. Csonka, J. M. Pitarke, *Phys. Rev. Lett.* **2012**, 109, 233203.
- [62] M.-Y. Chiu, U.-S. Jeng, M.-S. Su, K.-H. Wei, *Macromolecules* **2010**, 43, 428.
- [63] R. Hosemann, W. Vogel, D. Weick, F. J. Baltá-Calleja, *Acta Crystallogr. A* **1981**, 37, 85.
- [64] S. Engmann, F. A. Bokel, A. A. Herzing, H. W. Ro, C. Giroto, B. Caputo, C. V. Hoven, E. Schaible, A. Hexemer, D. M. DeLongchamp, L. J. Richter, *J. Mater. Chem. A* **2015**, 3, 8764.
- [65] E. F. Manley, T. Harschneck, N. D. Eastham, M. J. Leonardi, N. Zhou, J. Strzalka,
- [66] E. F. Manley, J. Strzalka, T. J. Fauvell, T. J. Marks, L. X. Chen, *Adv. Energy Mater.* **2018**, 8, 1.
- [67] L. A. Perez, K. W. Chou, J. A. Love, T. S. Van Der Poll, D. M. Smilgies, T. Q. Nguyen, E. J. Kramer, A. Amassian, G. C. Bazan, *Adv. Mater.* **2013**, 25, 6380.
- [68] E. Verploegen, R. Mondal, C. J. Bettinger, S. Sok, M. F. Toney, Z. Bao, *Adv. Funct. Mater.* **2010**, 20, 3519.
- [69] G. Benecke, W. Wagermaier, C. Li, M. Schwartzkopf, G. Flucke, R. Hoerth, I. Zizak, M. Burghammer, E. Metwalli, P. Müller-Buschbaum, M. Trebbin, S. Förster, O. Paris, S. V. Roth, P. Fratzl, *J. Appl. Crystallogr.* **2014**, 47, 1797.
- [70] M. Rauscher, T. Salditt, H. Spohn, *Phys. Rev. B* **1995**, 52, 16855.
- [71] C. Durniak, M. Ganeva, G. Pospelov, W. Van Herck, J. Wuttke, BornAgain, <http://www.bornagainproject.org> (accessed: June 2019).